PROCEEDINGS A

royalsocietypublishing.org/journal/rspa

Research

Cite this article: Browning AP, Woodhouse FG, Simpson MJ. 2019 Reversible signal transmission in an active mechanical metamaterial. *Proc. R. Soc. A* **475**: 20190146. http://dx.doi.org/10.1098/rspa.2019.0146

Received: 7 March 2019
Accepted: 11 June 2019

Subject Areas:
applied mathematics, mathematical modelling, biomechanics

Keywords:
active matter, metamaterial, mechanical signal transmission, travelling wave, FitzHugh–Nagumo model

Author for correspondence:
Matthew J. Simpson
e-mail: matthew.simpson@qut.edu.au

Electronic supplementary material is available online at https://dx.doi.org/10.6084/m9.figshare.c.4563902.

THE ROYAL SOCIETY PUBLISHING

Reversible signal transmission in an active mechanical metamaterial

Alexander P. Browning[1,2], Francis G. Woodhouse[3] and Matthew J. Simpson[1]

[1]Mathematical Sciences, and [2]ARC Centre of Excellence for Mathematical and Statistical Frontiers, Queensland University of Technology, Brisbane, Australia
[3]Mathematical Institute, University of Oxford, Oxford, UK

APB, 0000-0002-8753-1538; MJS, 0000-0001-6254-313X

Mechanical metamaterials are designed to enable unique functionalities, but are typically limited by an initial energy state and require an independent energy input to function repeatedly. Our study introduces a theoretical active mechanical metamaterial that incorporates a biological reaction mechanism to overcome this key limitation of passive metamaterials. Our material allows for reversible mechanical signal transmission, where energy is reintroduced by the biologically motivated reaction mechanism. By analysing a coarse-grained continuous analogue of the discrete model, we find that signals can be propagated through the material by a travelling wave. Analysis of the continuum model provides the region of the parameter space that allows signal transmission, and reveals similarities with the well-known FitzHugh–Nagumo system. We also find explicit formulae that approximate the effect of the time scale of the reaction mechanism on the signal transmission speed, which is essential for controlling the material.

1. Introduction

Mechanical metamaterials are artificially constructed and have mechanical properties defined by their structure [1]. Simple metamaterials consist of a one-, two- or three-dimensional array of elements connected by links [1–3] that may be elastic [4–7], magnetic [8,9] or electrostatic [4]. Mechanical metamaterials are highly tuneable [10–12] and by altering the

structure of these elements, and the properties of the links, materials have been developed that selectively transmit signals [13,14], behave as logic gates [5,15] or buckle after the application of an external stimulus [2]. There are many recent studies that experimentally realize simple mechanical metamaterials [6,14,16–19]. An advantage of these designs is that they are often well suited to using three-dimensional printing technology [3,5,16,18,20]; however, a common theme among existing metamaterials is that they generally require an external source of energy to be provided in order to power their functions [5,21]. Many existing technologies can be thought of as *static* or *inactive* in the sense that they are limited by a fixed initial energy state, and are only able to respond to a finite number of stimuli before the manual introduction of external energy.

Recent mathematical and experimental work has examined the properties of a class of one-dimensional bistable metamaterials [4,5]. These systems comprise elements, each of which consists of a mass connected to an external wall by a set of elastic elements that produce a bistable elastic potential. Individual elements are arranged in a one-dimensional lattice and are interconnected by linear springs (figure 1*a*). These elements may be tuned so that the elastic potential energy function is asymmetric, resulting in both a high and low potential energy stable configuration for each element (figure 1*b*). The system can, therefore, be designed so that an external stimulus, for example the change of a single node from the high to low potential energy stable state, can trigger a change in element configuration through the entire lattice [5]. This change is the transmission of a mechanical signal powered by stored elastic potential energy.

A limitation of this mechanical regime is that the system must receive an external energy input before the transmission of an additional signal [3,5]. Stiffness grading has been shown to overcome this limitation by exploiting a symmetric potential function [3]; however, these techniques may not allow the propagation of waves in systems with non-zero damping. The material in its current state is reset by manually moving each element back into its high potential energy configuration [5]. Our study introduces a theoretical biologically inspired mechanism that automatically resets each element to a high potential energy state, allowing the transmission of further signals. Many recent studies introduce the idea of manipulating biological subsystems in materials [22–24], or discuss behaviours that arise in *active matter* systems, where biological systems exert mechanical forces [25]. Some systems are biologically inspired [21,23,24] where properties of the metamaterial are designed to mimic a biological phenomenon, and some systems exploit the properties of biological subsystems to produce new behaviours in the material [22]. One possibility for our mechanism is to exploit actin filaments in eukaryotic cells [26–29] to convert energy provided to the cells as nutrients through chemical hydrolysis [30] into mechanical energy which can reset the bistable elements to a high potential energy configuration. The application of actin filaments in nanotechnology is well studied [28] and their exploitation in metamaterials has been previously suggested [29,30].

The biological reaction mechanism we introduce is designed to react to changes in the displacement of individual elements and respond by inducing elastic potential energy back into each element. Mathematically, the effect of this process is to reset the potential function so that each element eventually reverts to a high potential energy state, as shown in figure 1*b–d*. We present a mathematical characterization of this reaction mechanism and explore how the time scale of the reaction mechanism affects the ability of the system to transmit signals. We find that signal transmission through a coarse-grained description of the material takes the form of a travelling wave. Using a travelling wave model, we find explicit formulae that bound the parameter space for which signal transmission can occur, and approximate the effect the time scale of the reaction mechanism has on the signal transmission speed. We lay the foundation for future work on this system where the metamaterial can be tuned to produce useful new behaviours. The results we provide quantify the trade-off between the signal transmission speed and the time scale of the biological response, which are essential for control and tuning of the material. For clarity, throughout this work, we refer to the system without the reaction mechanism as the *inactive* system, and the system that includes the biological reaction mechanism as the *active* system.

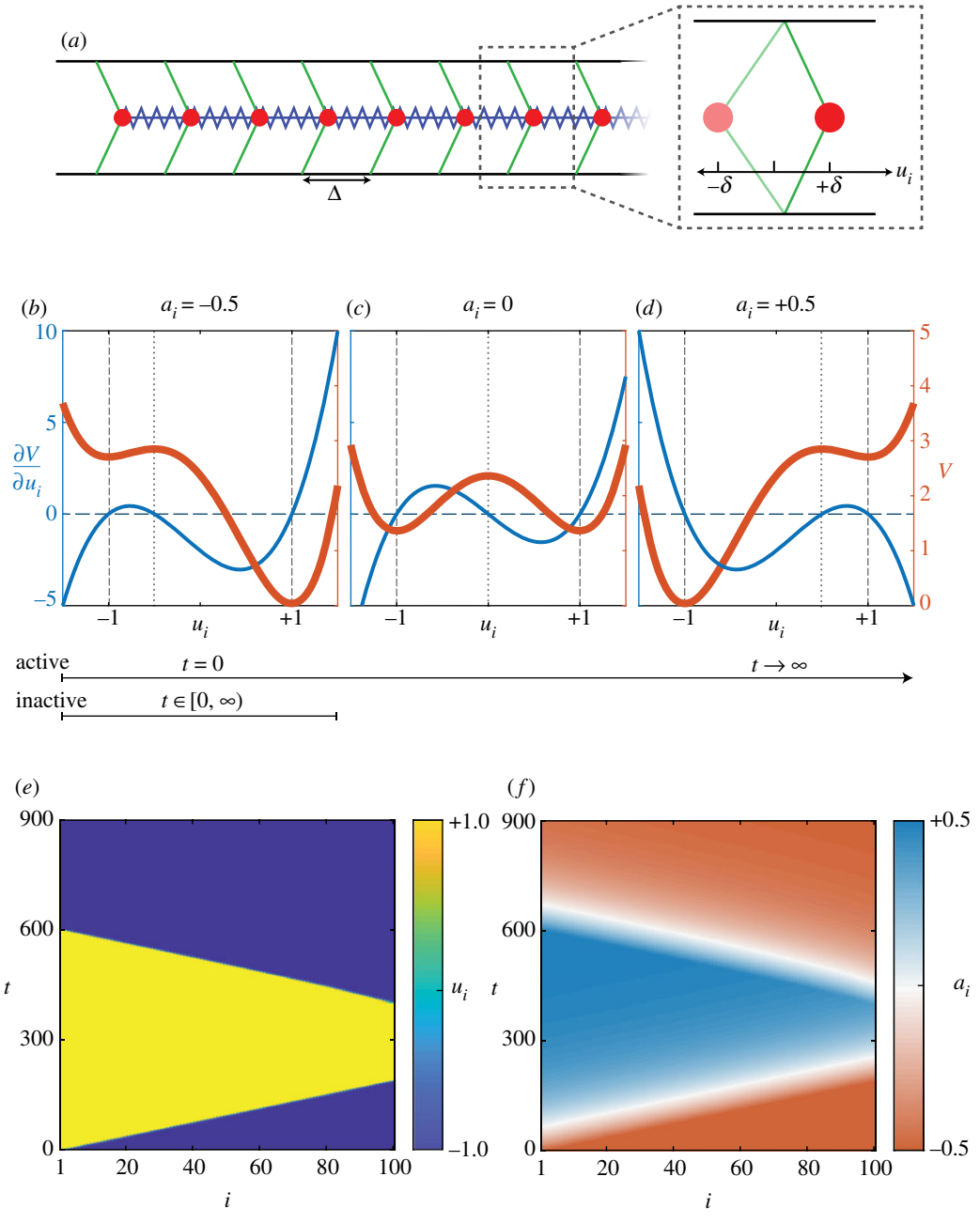

Figure 1. (*a*) Schematic of the one-dimensional metamaterial [5]. Each element (red), of mass m, has a natural spacing of Δ. Each mass is connected to an external wall by a bistable elastic element (green) and to neighbouring elements by linear elastic springs (blue). The inset shows both stable states for each element, $u_i(t) = \pm\delta$ where i is the mass index. (*b*) An example of bistable potential function (red) and its derivative (blue) for $a_i = -0.5$ and $\delta = 1$ in the inactive model, or the active model at $t = 0$. (*b–d*) The effect of the biological reaction mechanism, which resets the potential function. Note that (*d*) corresponds to a reflection of (*b*) about $u_i = 0$. For each plot, the stable steady states (dashed grey) and unstable steady state (dotted grey) are shown. (*e,f*) Signal propagation through this material showing (*e*) the displacement of each element, $u_i(t)$, and (*f*) the biological reaction, $a_i(t)$. The signal was initiated by moving the first element from a displacement of $-\delta$ to δ at $t = 0$, and was retransmitted by moving the last element from a displacement of δ to $-\delta$ at $t = 400$. We note the original signal could also be initiated from the right boundary by moving the last element from a displacement of $-\delta$ to δ, or indeed anywhere in the domain. Parameters used are $m = 1$ g, $k = 1$ g m s^{-2}, $\gamma = 1$ g s^{-1}, $\Delta = 0.002$ m, $\delta = 1$ m, $\epsilon = 0.01$/s, $\eta = 2$, $v = 1$ g/(m^2 s^2) and $N = 101$ masses. (Online version in colour.)

In §2, we present a mathematical model that describes the discrete active mechanical system. Following this, we take a continuous limit of the discrete model [4] with which we qualitatively explore the effect of the reaction mechanism on the ability of the system to transmit mechanical signals. We find evidence of travelling waves in the continuous model, where the wavespeed corresponds to the signal transmission speed. In §3, we solve for the wavespeed and shape in the case where the reaction mechanism is excluded. This analysis is then extended to explore the effect that the reaction mechanism has on the wavespeed and shape by taking a singular perturbation expansion (§§3a) and applying an energy conservation argument (§§3b). Finally, in §4, we discuss and summarize our results, and outline future work involving our active metamaterial.

2. Mathematical model

The metamaterial presented by Raney *et al.* [5] consists of N bistable elements of mass m, interconnected by $N-1$ linear springs of stiffness k; each of the bistable elements is attached to two external walls by a pair of elastic elements, with a separation of Δ. A schematic of this physical system is shown in figure 1*a*. Denoting the displacement of the ith mass relative to the mean of its two steady states as $u_i(t)$, the state of the discrete system is governed by

$$\left.\begin{aligned} 0 &= m\frac{\mathrm{d}^2u_i}{\mathrm{d}t^2} - k(u_{i+1} - u_i - \Delta) + \gamma\frac{\mathrm{d}u_i}{\mathrm{d}t} + \frac{\partial V}{\partial u_i}, \quad i = 1, \\ 0 &= m\frac{\mathrm{d}^2u_i}{\mathrm{d}t^2} - k(u_{i+1} - 2u_i + u_{i-1}) + \gamma\frac{\mathrm{d}u_i}{\mathrm{d}t} + \frac{\partial V}{\partial u_i}, \quad i = 2, \ldots, N-1 \\ \text{and} \quad 0 &= m\frac{\mathrm{d}^2u_i}{\mathrm{d}t^2} - k(u_i - u_{i-1} + \Delta) + \gamma\frac{\mathrm{d}u_i}{\mathrm{d}t} + \frac{\partial V}{\partial u_i}, \quad i = N, \end{aligned}\right\} \tag{2.1}$$

where γ is a damping parameter and $V(u_i, a_i)$ describes the potential energy of the bistable elements that connect each mass to the external wall [4,5].

In this study, we choose $V(u_i, a_i)$ to be a quartic [4] defined in terms of its derivative,

$$\frac{\partial V}{\partial u_i} = v(u_i^2 - \delta^2)(u_i - a_i), \tag{2.2}$$

where v describes the stiffness of the bistable elements and relates to the size of the energy gap between high and low potential energy configurations, $u_i = \pm\delta$ are the stable fixed points of $V(u_i, a_i)$ and $u_i = a_i \in [-\delta, \delta]$ is the unstable fixed point which governs the symmetry of $V(u_i, a_i)$ (figure 1*b*). For this choice of potential energy function, $u_i = \mathrm{sign}(a_i)\delta$ corresponds to an element in the high potential energy configuration and $u_i = -\mathrm{sign}(a_i)\delta$ corresponds to an element in the low potential energy configuration (figure 1*b*).

In our study, we allow the symmetry of the potential function to vary in reaction to changes in the displacement, $u_i(t)$, by allowing $a_i = a_i(t)$ and enforcing

$$\frac{\mathrm{d}a_i}{\mathrm{d}t} = \epsilon\left(\frac{u_i}{\eta} - a_i\right). \tag{2.3}$$

Physically, a_i represents a biological subsystem that receives energy from external sources and induces it into the material at a rate proportional to ϵ. The parameter $\eta > 1$ determines the extrema of the reaction parameter so that $a_i(t) \in [-\delta/\eta, \delta/\eta]$. This implementation means that if a user transmits a signal through the material by changing the displacement of a node (figure 1*e*), and waits a period of time of $\mathcal{O}(\epsilon^{-1})$ after the signal reaches the end of the domain, all elements of the system will have reverted to their high potential energy states. This resetting process of $a_i(t)$, and by extension $V(u_i, a_i)$, is shown for a single element in figure 1*b–d*, and throughout the material in figure 1*f*. The discrete system is similar to other fast–slow bistable systems, such as the FitzHugh–Nagumo model [31–33]. In this context, we consider that the displacement function, $u_i(t)$, undergoes an excitable excursion in phase space in response to an external stimulus, and the variable representing the biological response, $a_i(t)$, behaves as a linear recovery variable. In

addition to the results in figure 1*e*, we reproduce results in the electronic supplementary material, in the case that the second signal is initiated too early, so propagation cannot occur.

If the length of the material is large relative to the separation of each mass, Δ, we can describe the material with a coarse-grained continuous model [34]. To derive a continuous description of the system described by equation (2.1), we consider a material of fixed length, $L = (N-1)\Delta$, and take the limit $N \to \infty$ so that $\Delta \to 0$. Following this, we define field functions $u(x,t)$ and $a(x,t)$ that describe $u_i(t)$ and $a_i(t)$, respectively, for $x = (i-1)\Delta \in (0, L)$. When taking a continuous limit of the discrete system we require that the macroscopic quantities in the discrete model remain $\mathcal{O}(1)$ for physical reasons [4]. To do this, we replace unit quantities m, v and γ with density quantities, $\rho = m/\Delta$, $\hat{v} = v/\Delta$ and $\hat{\gamma} = \gamma/\Delta$, respectively, and scale the connecting spring force, $\hat{k} = \Delta k$.

Dividing equation (2.1) by Δ and taking the limit $\Delta \to 0$ results in the continuous model,

$$0 = \rho \frac{\partial^2 u}{\partial t^2} - \hat{k} \frac{\partial^2 u}{\partial x^2} + \hat{\gamma} \frac{\partial u}{\partial t} + \hat{v}(u^2 - \delta)(u - a) = 0 \tag{2.4}$$

and

$$0 = \frac{\partial a}{\partial t} - \epsilon \left(\frac{u}{\eta} - a \right). \tag{2.5}$$

A no flux boundary condition $\partial u/\partial x = 0$ is applied at $x = 0$ and $x = L$.

A key aspect of this study is to investigate the signal transmission speed through the parameter space, particularly as ϵ increases. We therefore non-dimensionalize equations (2.4) and (2.5) by scaling $t = T\hat{t}$, $x = X\hat{x}$, $u = U\hat{u}$ and $a = A\hat{a}$, where hat notation represents dimensionless variables. Choosing $U = A = \delta$, $T^2 = \rho/\hat{\gamma}$ and $X^2 = \hat{k}T^2/\rho$ gives

$$0 = \frac{\partial^2 \hat{u}}{\partial \hat{t}^2} - \frac{\partial^2 \hat{u}}{\partial \hat{x}^2} + \frac{\partial \hat{u}}{\partial \hat{t}} + \nu(\hat{u}^2 - 1)\left(\frac{\hat{u}}{\eta} - \hat{a} \right) \tag{2.6}$$

and

$$0 = \frac{\partial \hat{a}}{\partial \hat{t}} - \kappa \left(\frac{\hat{u}}{\eta} - \hat{a} \right), \tag{2.7}$$

where $\kappa = T\epsilon \geq 0$, $\nu = \hat{v}\delta^2\rho/\hat{\gamma}^2 > 0$, $\eta > 1$ and $\hat{x} \in (0, \hat{L})$. The behaviour of the system can now be studied through the three-dimensional parameter space (ν, η, κ), where $\nu > 0$ is the relative strength of the potential function; $\eta > 1$ describes the steady-state locations of $\hat{a}(\hat{x}, \hat{t})$; and $\kappa \geq 0$ is the relative time scale of the reaction mechanism. In this non-dimensional regime, the stable states are located at $\hat{u} = \pm 1$, where the high potential energy state is always given by $\text{sign}(\hat{a})$.

Previous studies provide evidence to suggest that the transmitted energy is input independent [35], so we do not expect the initial condition to affect the transmission speed in the centre of the domain. A signal is initiated in the continuous model using a Heaviside initial condition for the displacement, where

$$\hat{u}(\hat{x}, 0) = \begin{cases} 1, & 0 \leq \hat{x} < Q, \\ -1, & Q \leq \hat{x} \leq \hat{L}, \end{cases} \tag{2.8}$$

and the biological response is kept as it was before the signal was initiated by setting

$$\hat{a}(\hat{x}, 0) = -\frac{1}{\eta}. \tag{2.9}$$

In figure 2*a*, numerical solutions to the continuous model show that the transition of the displacement variable, $\hat{u}(\hat{x}, \hat{t})$, is carried by a wave which appears to approach a constant shape and speed. Figure 2*b* demonstrates the slow biological response, where $\hat{a}(\hat{x}, \hat{t})$ also undergoes a slow transition in response to changes in $\hat{u}(\hat{x}, \hat{t})$. Results in figure 3 illustrate the dependence of the transmission speed on the time scale of the response, κ. These results indicate a negative monotonic relationship between κ and the transmission speed. Full details of the numerical scheme used to solve the continuous model are provided in the electronic supplementary material.

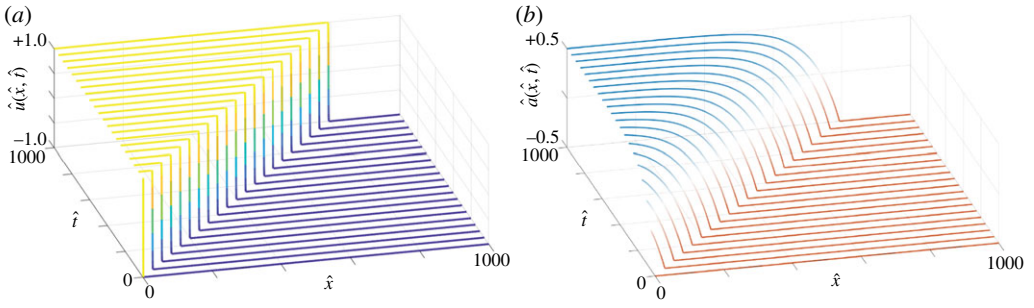

Figure 2. Numerical solutions to the non-dimensional continuous model (equations (2.6) and (2.7)) showing (*a*) the displacement field, $\hat{u}(\hat{x},\hat{t})$, and (*b*) the biological reaction, $\hat{a}(\hat{x},\hat{t})$. Parameters used are $\nu = 4$, $\eta = 2$ and $\kappa = 0.01$. The signal is initiated using the initial condition described by equations (2.8) and (2.9) with $Q = 1$. (Online version in colour.)

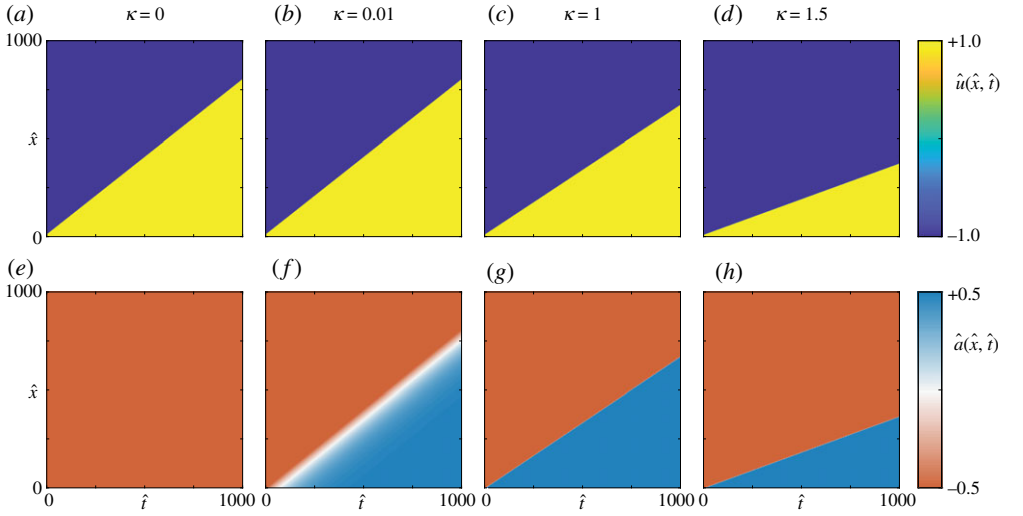

Figure 3. The solution to the continuous model, equation (2.6), shown as kymographs where colouring represents (*a–d*) the displacement function, $\hat{u}(\hat{x},\hat{t})$, and (*e–h*) the biological response, $\hat{a}(\hat{x},\hat{t})$, for increasing values of κ. Parameter values used are $\nu = 4$ and $\eta = 2$. Each signal is initiated using the initial condition described by equations (2.8) and (2.9) with $Q = 1$. (Online version in colour.)

3. Travelling wave model

Figure 2 suggests that signals are propagated through the system by waves which appear to approach a constant shape and speed. Motivated by this, we now look for a travelling wave solution to the continuous model by extending the domain to represent a material of infinite length, so that $\hat{x} \in \mathbb{R}^+$ [3,4,32,33,36–42]. We define the wavespeed, c, and without loss of generality enforce $c > 0$ by investigating travelling waves that are initiated at the left boundary and move in only the positive $\hat{x}$ direction. In reality, we expect symmetry in these solutions as a travelling wave may also travel in the negative $\hat{x}$ direction if the signal is initiated in the centre of the domain.

Substituting travelling wave variables $f(z) = \hat{u}(\hat{x},\hat{t})$ and $h(z) = \hat{a}(\hat{x},\hat{t})$, where $z = \hat{x} - c\hat{t} \in \mathbb{R}$, into equations (2.6) and (2.7), and dividing by $c^2 - 1$, gives the travelling wave model,

$$0 = \frac{\mathrm{d}^2 f}{\mathrm{d}z^2} + \frac{c}{1-c^2}\frac{\mathrm{d}f}{\mathrm{d}z} - \frac{\nu}{1-c^2}(f^2-1)(f-h), \quad f(\pm\infty) = \mp 1 \tag{3.1}$$

and

$$0 = \frac{\mathrm{d}h}{\mathrm{d}z} + \frac{\kappa}{c}\left(\frac{f}{\eta} - h\right), \quad h(\infty) = -\frac{1}{\eta}, \tag{3.2}$$

which, in physical coordinates, corresponds to a wave profile connecting $\hat{u} = -1$ to $\hat{u} = 1$ as $t \to \infty$.

In figure 3, numerical solutions of the continuous model show that increasing the response speed κ typically reduces the wavespeed from a maximum which occurs when $\kappa = 0$. We, therefore, denote a *fast wave* as a travelling wave solution at, or near, $\kappa = 0$, and a *slow wave* as a travelling wave solution in the limit, or near, $c = 0$. Removing the active component of the system from the model by setting $\kappa = 0$ (and defining c_0 as the corresponding wavespeed) gives

$$0 = \frac{\mathrm{d}^2 f_0}{\mathrm{d}z^2} + \frac{c_0}{1 - c_0^2}\frac{\mathrm{d}f_0}{\mathrm{d}z} - \frac{\nu}{1 - c_0^2}(f_0^2 - 1)\left(f_0 + \frac{1}{\eta}\right), \quad f_0(\pm\infty) = \mp 1 \tag{3.3}$$

and

$$0 = \frac{\mathrm{d}h_0}{\mathrm{d}z}, \quad h_0(\infty) = -\frac{1}{\eta}, \tag{3.4}$$

where $f_0(z)$ will correspond to the solution to the fast wave. Under certain parameter transformations, equation (3.3) is analogous to the well-studied bistable equation that arises from analysis of the FitzHugh–Nagumo model [31–33,38]. The solution of equations (3.3) and (3.4) is therefore

$$f_0(z) = -\tanh(\mu_0 z) \tag{3.5}$$

and

$$h_0(z) = -\frac{1}{\eta}, \tag{3.6}$$

where

$$\mu_0 = \sqrt{\frac{\nu^2}{\eta^2} + \frac{\nu}{2}} \quad \text{and} \quad c_0 = \sqrt{\frac{1}{(\eta^2/2\nu + 1)}}. \tag{3.7}$$

For physically realistic parameter combinations, equation (3.7) suggests that $c_0 < 1$.

(a) Perturbation solution for the fast wave

An exact solution in the limiting case $\kappa = 0$ (equation (3.5)) allows the formulation of a perturbation solution for $0 < \kappa \ll 1$ [38,39,43]. Figure 4 shows an approximation to the wave profiles $f(z)$ and $h(z)$ for $\kappa = 0.01$. A fast transition region is seen in $f(z)$ around $z = 0$ (figure 4*a*), suggesting behaviour necessitating a singular perturbation analysis [39,43]. For $z \sim \mathcal{O}(\mu_0^{-1})$, the solution appears to match a solution for $\kappa = 0$, since, at this scale, $h(z)$ is approximately constant (figure 4*b*). In figure 4*a*, we show that $h(z)$ is not constant but rather a slow reaction of $\mathcal{O}(\kappa^{-1})$, which transitions $h(z) = -1/\eta$ to $h(z) = 1/\eta$ as $z \to -\infty$. This observation further suggests a singular perturbation analysis, since the behaviour of the response mechanism $h(z)$ varies significantly for $0 < \kappa \ll 1$ compared with $\kappa = 0$.

We propose a three-part perturbation solution about $\kappa = 0$ and define independent variables $z \sim \mathcal{O}(\mu_0^{-1})$ to correspond to an *inner region*, and $Z = \kappa z$ for $z \sim \mathcal{O}(\kappa^{-1})$ to correspond to two *outer regions*. These three regions are shown in figure 4*a*. This regime requires the fast process, which occurs in the inner region, to be much faster than the slow process, which occurs in the outer region. That is, we require $\kappa \ll \mu_0$.

Our aim in looking for a perturbation solution is to determine the effect of small perturbations in κ on c. To do this, we pose a perturbation expansion for the wavespeed through the entire domain,

$$c = c_0 + c_1\kappa + \mathcal{O}(\kappa^2), \tag{3.8}$$

where c_0 is given by equation (3.7).

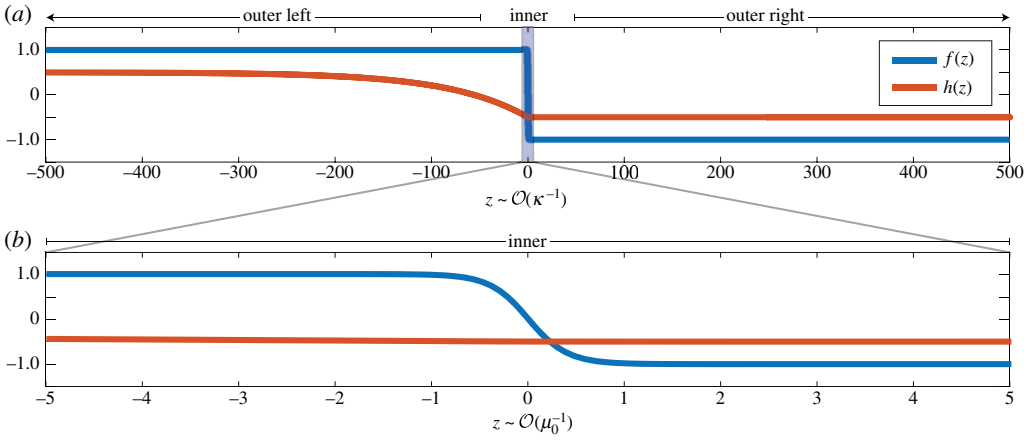

Figure 4. Approximation of the travelling wave profile using a solution to the continuous model for (*a*) the displacement function, $f(z)$, and (*b*) the biological reaction, $h(z)$. Parameters used are $\nu = 4$, $\eta = 2$ and $\kappa = 0.01$. In (*a*), the horizontal axis is scaled to show both outer regions where $z \sim \mathcal{O}(\kappa^{-1})$, which is the rate of change of $h(z)$. In (*b*), the horizontal axis is scaled to show the inner region where $z \sim \mathcal{O}(\mu_0^{-1})$, which is the rate of change of $f(z)$. (Online version in colour.)

In the inner region, we pose a perturbation solution of the form

$$f(z) = f_0(z) + f_1(z)\kappa + \mathcal{O}(\kappa^2) \tag{3.9}$$

and

$$h(z) = h_0(z) + h_1(z)\kappa + \mathcal{O}(\kappa^2), \tag{3.10}$$

where $f_0(z)$ and $h_0(z)$ correspond to the shape of the fast wave at $\kappa = 0$, given by equation (3.5). Full details of the perturbation solution in the inner region are given in the electronic supplementary material. In summary, the solution is given by

$$f(z) = -\tanh(\mu_0 z) + f_1(z)\kappa + \mathcal{O}(\kappa^2) \tag{3.11}$$

and

$$h(z) = -\frac{1}{\eta} + \frac{1}{c_0\mu_0\eta}\Big(\log(\cosh(\mu_0 z)) - \mu_0 z + \log(2)\Big)\kappa + \mathcal{O}(\kappa^2), \tag{3.12}$$

where $f_1(z)$ and c_1 are defined by the solution of a second-order boundary value problem, which can be solved numerically. Full details of this numerical scheme are given in the electronic supplementary material. These solutions are shown in figure 5, and the wavespeed correction, c_1, is summarized for various parameter combinations in electronic supplementary material, table S3.

In the outer region, we denote solutions to the slow system using uppercase variables, $F(Z)$ and $H(Z)$. We expect the outer solution to apply for $Z \sim \mathcal{O}(1) \Rightarrow z \sim \mathcal{O}(\kappa^{-1})$ and as $z, Z \to \infty$. In the outer region, equation (3.1) becomes

$$0 = \kappa^2 \frac{\mathrm{d}^2 F}{\mathrm{d}Z^2} + \frac{c\kappa}{1-c^2}\frac{\mathrm{d}F}{\mathrm{d}Z} - \frac{\nu}{1-c^2}(F^2-1)(F-H), \quad F(\pm\infty) = \mp 1, \tag{3.13}$$

which has the solution

$$F(Z) = -\mathrm{sign}(Z). \tag{3.14}$$

This agrees with the sharp transition region seen at this scale in figure 4*a*. Substituting equation (3.14) into equation (3.2) we see that

$$0 = \frac{\mathrm{d}H}{\mathrm{d}Z} - \frac{1}{c}\left(\frac{\mathrm{sign}(Z)}{\eta} + H\right), \quad H(\infty) = -\frac{1}{\eta}. \tag{3.15}$$

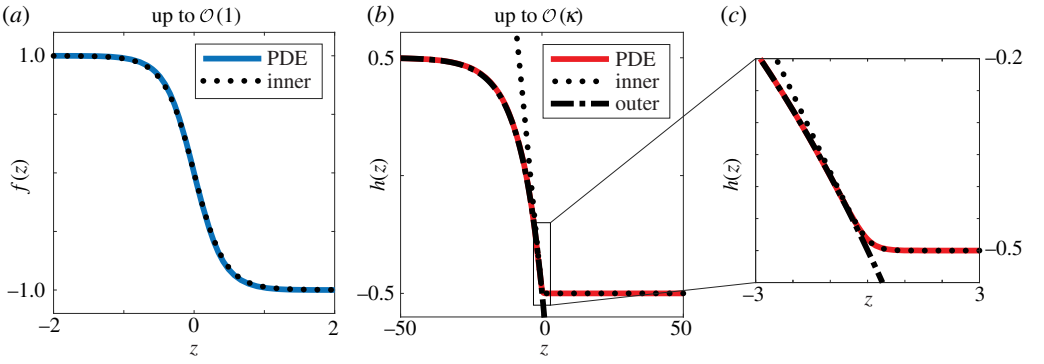

Figure 5. Comparison of the wave shape from a numerical solution to the continuous model (coloured solid curves) with the perturbation solution (black dotted and dotted-dashed curves) for (*a*) the displacement function, $f(z)$, to $\mathcal{O}(1)$ and (*b*) the reaction mechanism, $h(z)$, to $\mathcal{O}(\kappa)$. The inset (*c*) shows the crossover between the inner and outer perturbation solutions to $h(z)$ in further detail, showing an excellent match to the wave shape from the continuous model, and between the inner and outer solutions. (Online version in colour.)

Full details of the perturbation solution in the outer region are given in the electronic supplementary material. In summary, the solution to equation (3.15) is given by

$$H(Z) = \begin{cases} \dfrac{1}{\eta} - \dfrac{2}{\eta}\exp\left(\dfrac{Z}{c_0}\right) - \dfrac{2c_1}{\eta c_0^2} Z \exp\left(\dfrac{Z}{c_0}\right)\kappa + \mathcal{O}(\kappa^2), & Z < 0, \\ -\dfrac{1}{\eta}, & Z > 0. \end{cases} \tag{3.16}$$

Figure 5*b–c* shows a comparison between solutions for the reaction mechanism in the inner and outer regions (given by equations (3.11) and (3.16), respectively) and an approximation of the wave shape formed from the numerical solution to the continuous model. We see an excellent match between both the continuous model and the perturbation solutions, as well as between the inner and outer regions of the perturbation solution. These results provide excellent information about the behaviour of $h(z)$ for $0 < \kappa \ll 1$, and are particularly important as the behaviour for $0 < \kappa \ll 1$ varies significantly from the behaviour at $\kappa = 0$.

(b) Energy transport

To determine information about the slow wave, and to obtain more information about the fast wave, we follow Nadkarni *et al.* [4,41] to derive an integrability condition—that is, a necessary condition for the existence of a solution with given boundary conditions—to investigate the transported energy. Multiplying the travelling wave model, given by equation (3.1), by $\mathrm{d}f/\mathrm{d}z$ and integrating gives

$$0 = \int_{-\infty}^{\infty} \frac{\mathrm{d}^2 f}{\mathrm{d}z^2}\frac{\mathrm{d}f}{\mathrm{d}z}\,\mathrm{d}z + \frac{c}{1-c^2}\int_{-\infty}^{\infty}\left(\frac{\mathrm{d}f}{\mathrm{d}z}\right)^2 \mathrm{d}z - \frac{\nu}{1-c^2}\int_{-\infty}^{\infty}(f^2-1)(f-h)\frac{\mathrm{d}f}{\mathrm{d}z}\,\mathrm{d}z. \tag{3.17}$$

For a parameter regime where the transition wave exists, the velocity will vanish in the far field so that $f \to \mp 1$ and $\mathrm{d}f/\mathrm{d}z \to 0$ as $z \to \pm\infty$. Therefore, some components of equation (3.17) vanish,

$$\int_{-\infty}^{\infty} \frac{\mathrm{d}^2 f}{\mathrm{d}z^2}\frac{\mathrm{d}f}{\mathrm{d}z}\,\mathrm{d}z = \left[\frac{1}{2}\left(\frac{\mathrm{d}f}{\mathrm{d}z}\right)^2\right]_{-\infty}^{\infty} = 0$$

and

$$\int_{-\infty}^{\infty}(f^2-1)(f-h)\frac{\mathrm{d}f}{\mathrm{d}z}\,\mathrm{d}z = -\int_{-\infty}^{\infty}\frac{\mathrm{d}f}{\mathrm{d}z}(f^2-1)h\,\mathrm{d}z.$$

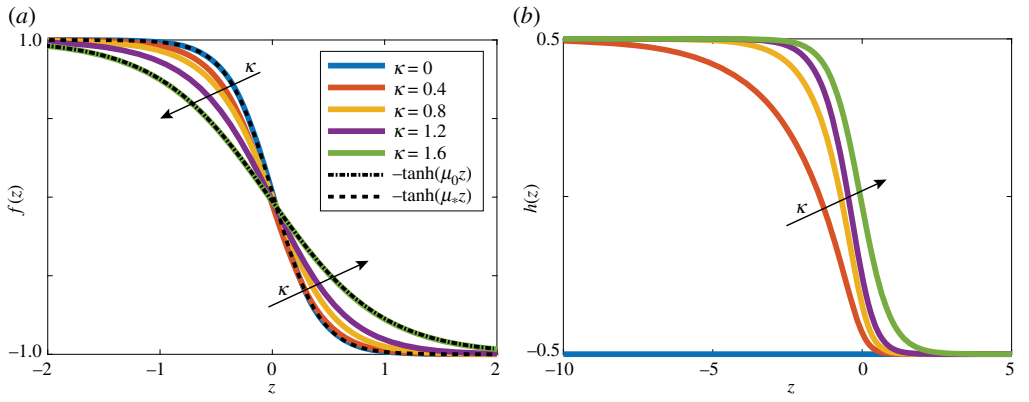

Figure 6. Approximate numerical solutions to the travelling wave model, formulated from numerical solutions to the continuous model, for (*a*) the displacement function, $f(z)$, and (*b*) the biological reaction, $h(z)$. Results are shown for various values of the response parameter, κ, with $\nu = 4$ and $\eta = 2$. Additionally, (*a*) shows the exact solutions to the travelling wave model, equations (3.1) and (3.2), for $\kappa = 0$ (black dashed-dot) and $\kappa = \kappa_* = 1.6$ (black dashed). (Online version in colour.)

Under the assumption $|c| \neq 1$, equation (3.17) becomes an *integrability condition*,

$$c\int_{-\infty}^{\infty}\left(\frac{\mathrm{d}f}{\mathrm{d}z}\right)^2 \mathrm{d}z = -\nu\int_{-\infty}^{\infty}\frac{\mathrm{d}f}{\mathrm{d}z}(f^2-1)h\,\mathrm{d}z. \tag{3.18}$$

It is useful to note that, for $f = -\tanh(\sigma z)$, for some σ, which occurs as $\kappa \to 0$ with $\sigma = \mu_0$,

$$(f^2-1)\frac{\mathrm{d}f}{\mathrm{d}z}h \propto \mathrm{sech}^4(\sigma z)h. \tag{3.19}$$

This suggests that only the component of $h(z)$ near $z = 0$ is important in gaining any approximation from the integrability condition, provided $f(z)$ has the form of a hyperbolic tangent function. Since a travelling wave connecting $f(z) = 1$ to $f(z) = -1$ as $z \to \infty$ will always have a sigmoidal form (figure 6), we expect this observation to apply for all regions of the parameter space where a travelling wave exists.

In the inactive model, where $\kappa = 0$, Nadkarni *et al.* [4] show that the integrability condition reduces to

$$E_k = \frac{c\Delta V}{2\gamma}, \tag{3.20}$$

where E_k represents the total kinetic energy per density transported by the transition wave, and ΔV represents an *energy gap* or difference in the potential energy between the high and the low potential energy states. This result can be used to find an upper bound for c for $\kappa > 0$: since $|h(t)| \leq 1/\eta$ and ΔV is a monotonically decreasing function of $h(t)$, the available kinetic energy in the system is always bounded above by that which occurs when $h(t) \equiv 1/\eta$, which is the case for $\kappa = 0$. This suggests that $c(\kappa) \leq c_0 < 1$ and substantiates numerical evidence seen in figure 3, which suggests a decreasing monotonic relationship between c and κ.

In the following subsections, we apply the integrability condition to obtain approximations to $c(\kappa)$ while holding ν and η constant. We also find the region of the parameter space that allows signal transmission. The advantage of these approximations is that they avoid numerical solutions to the continuous model to approximate the wavespeed. Numerical solutions to this model are not computationally inexpensive and it is generally difficult to obtain and verify the results.

(i) Energy transport in the fast wave

For $\kappa \ll 1$, it is reasonable to assume that $f \approx -\tanh(\mu z)$, where μ depends on κ and $\mu \to \mu_0$ as $\kappa \to 0$. By assuming $f(z)$ has a similar form to $f_0(z)$ for $\kappa \ll 1$, it is reasonable to use the perturbation solution (equation (3.12)) as an approximation for $h(z)$. Since the integrability condition (equation (3.18)) depends only on the component of $h(z)$ near $z = 0$, we use only equation (3.12). Allowing $\mu_0 = \mu(0)$ and $c_0 = c(0)$, where $\mu = \mu(\kappa)$ and $c = c(\kappa)$ depend on κ, we assume that

$$h(z) \approx -\frac{1}{\eta} + \frac{\kappa}{c\mu\eta}\Big(\log(\cosh(\mu z)) - \mu z + \log(2)\Big), \quad \kappa \ll 1. \tag{3.21}$$

Equation (3.21) corresponds to the *smoothed* piecewise-defined function where growth is equal to $2\kappa/(c\eta)$ for $z < 0$, and zero for $z > 0$. This function corresponds exactly to an $\mathcal{O}(1)$ approximation to $h(z)$, which uses $f(z) = -\text{sign}(z)$. Substituting equation (3.21) into the integrability condition (equation (3.18)) provides the relationship

$$\frac{4c^2\mu^2}{3} = \frac{2\nu(6c\mu - 5\kappa)}{9\eta}. \tag{3.22}$$

This result does not allow c and μ to be determined independently, so we consider a far-field expansion of the travelling wave [36], that is, an expansion about $\phi \approx 0$, where $\phi = e^{-\mu z}$,

$$f(z) = -\tanh(\mu z) = \frac{e^{-2\mu z} - 1}{e^{-2\mu z} + 1} = \frac{\phi^2 - 1}{\phi^2 + 1} = -1 + 2\phi^2 + \mathcal{O}(\phi^4). \tag{3.23}$$

Substituting $\phi = e^{-\mu z}$ and equation (3.23) into the travelling wave equation for $h(z)$ (equation (3.2)) gives

$$\left.\begin{aligned} f(z) &\sim -1 + 2e^{-2\mu z}, \quad |z^{-1}| \ll 1 \\ \text{and} \qquad h(z) &\sim -\frac{1}{\eta} + \frac{2\kappa}{\eta(\kappa + 2c\mu)} e^{-2\mu z}, \quad |z^{-1}| \ll 1. \end{aligned}\right\} \tag{3.24}$$

Substituting equation (3.24) into equation (3.1) provides a far-field relationship,

$$0 = \frac{\nu}{\eta} - c\mu - \nu + 2\mu^2(1 - c^2). \tag{3.25}$$

To obtain a useful analytical expression for c and μ, we pose a perturbation solution to equations (3.22) and (3.25) around $\kappa = 0$, such that

$$c = c_0 + \tilde{c}_1\kappa + \mathcal{O}(\kappa^2) \tag{3.26}$$

and

$$\mu = \mu_0 + \tilde{\mu}_1\kappa + \mathcal{O}(\kappa^2), \tag{3.27}$$

where c_0 and μ_0 are given by equation (3.7). We note that $\tilde{c}_1$ approximates c_1, the gradient of $c(\kappa)$ at $\kappa = 0$, where c_1 is defined exactly by the solution of the perturbation problem. Substitution into equations (3.22) and (3.25) gives

$$\tilde{c}_1 = \frac{5\nu\left(4c_0^2\mu_0 + c_0 - 4\mu_0\right)}{24\mu_0^2\left(2c_0\eta\mu_0 - \nu\right)}. \tag{3.28}$$

We compare this estimate of c_1, which is calculated numerically by solving the boundary value problem that comes from the singular perturbation expansion, with that estimated from the continuous model in electronic supplementary material, table S3. In figure 7, we show that, for $\kappa \ll 1$,

$$c(\kappa) \sim c_0 + \tilde{c}_1\kappa \tag{3.29}$$

matches numerical results for $c(\kappa)$.

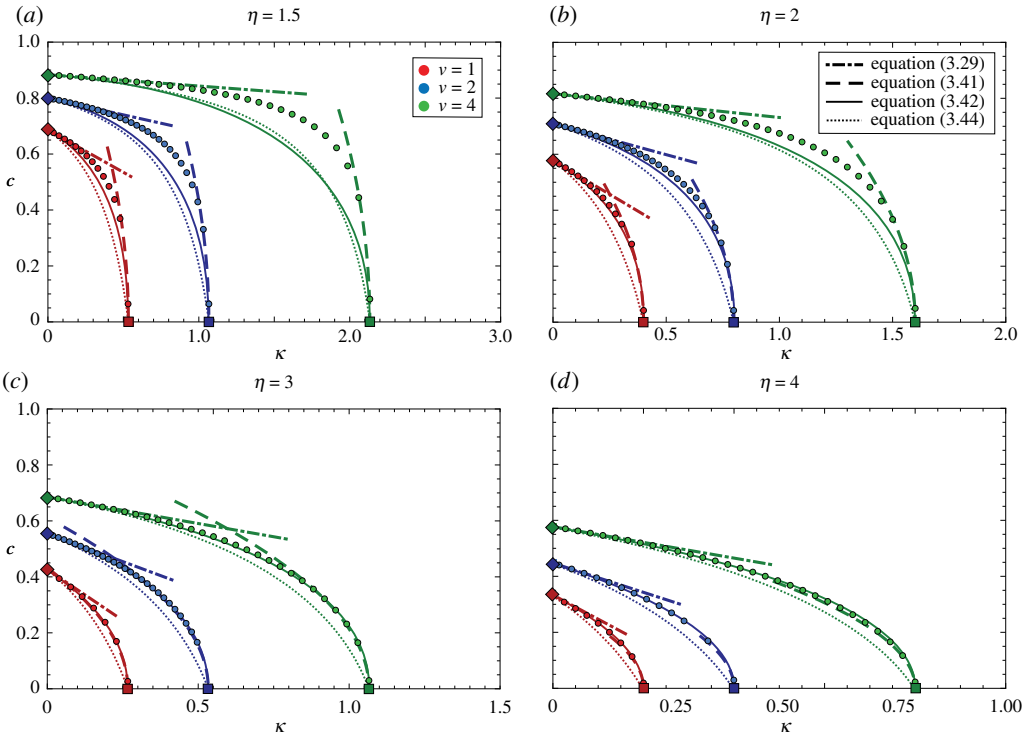

Figure 7. Comparison between the wavespeed as a function of κ, from the continuous model (circles), with: the analytical expression at $\kappa = 0$, given by equation (3.7) (diamonds); the analytical expression for κ_* at $c = 0$, given by equation (3.37) (squares); the analytical approximation given by equation (3.29), which applies for $\kappa \ll 1$ (dashed-dotted curve); the analytical approximation given by equation (3.41), which applies for $c \ll 1$ (dashed curve); the combined approximation given by equation (3.42), which applies everywhere (dotted curve); and the approximation given by equation (3.44), which applies everywhere (solid curve). (Online version in colour.)

(ii) Energy transport in the slow wave

We denote $f_*(z)$ and $h_*(z)$ as the shape of the slow wave, which occurs as $c \to 0$ and $\kappa \to \kappa_*$, where κ_* is yet to be determined. In addition, we expect the curve $c(\kappa)$ to be perpendicular to the κ axis at κ_* to maintain continuity in the symmetry of the problem where solutions with a negative wavespeed are equally valid. To determine a governing equation for the slow wave, we take $c \to 0$, so that equations (3.1) and (3.2) become

$$0 = \frac{\mathrm{d}^2 f_*}{\mathrm{d}z^2} - \nu\left(1 - \frac{1}{\eta}\right) f_*(f_*^2 - 1), \quad f_*(\pm\infty) = \mp 1 \tag{3.30}$$

and

$$0 = \frac{f_*}{\eta} - h_*, \tag{3.31}$$

which have the analytical solution

$$\left.\begin{aligned} f_*(z) &= -\tanh(\mu_* z) \\ \text{and} \quad h_*(z) &= -\frac{1}{\eta}\tanh(\mu_* z), \end{aligned}\right\} \tag{3.32}$$

where

$$\mu_* = \sqrt{\frac{\nu}{2}\left(1 - \frac{1}{\eta}\right)}. \tag{3.33}$$

Direct substitution of $f_*(z)$ and $h_*(z)$ into the integrability condition (equation (3.18)) causes all terms to vanish, so higher order behaviour of $\mathcal{O}(c)$ as $c \to 0$ is important. To allow for this, we note that equation (3.2) can be solved, for all κ, to give

$$h(z) = \frac{\kappa}{c\eta} \int_z^\infty f(s) \exp\left[\frac{\kappa}{c}(z-s)\right] \mathrm{d}s. \tag{3.34}$$

Equation (3.34) shows that $h(z)$ depends on the product of $f(s)$ and a function that decays rapidly as z moves away from s. Expanding $f(s)$ in a Taylor series about z gives

$$h(z) \approx \frac{\kappa}{c\eta} \int_z^\infty \left[\sum_{n=0}^{\infty} \frac{(s-z)^n}{n!} \frac{\mathrm{d}^n f}{\mathrm{d}z^n}\right] \exp\left(\frac{\kappa}{c}(z-s)\right) \mathrm{d}s = \frac{1}{\eta} \sum_{n=0}^{\infty} \frac{c^n}{\kappa^n} \frac{\mathrm{d}^n f}{\mathrm{d}z^n}. \tag{3.35}$$

Assuming that $f \sim \tanh(\mu(\kappa)z)$ provided $c \ll 1$, where $\mu(\kappa_*) = \mu_*$, and truncating the infinite series given by equation (3.35) after $n = 3$, the integrability condition (equation (3.18)) gives the relationship

$$\frac{4\kappa^3}{3} = \frac{16\nu\left(7\kappa^2 - 8c^2\mu^2\right)}{105\eta}. \tag{3.36}$$

For η and ν fixed, $c \to 0$ only as $\kappa \to \kappa_*$. Substituting $c = 0$ into equation (3.36) gives

$$\kappa_* = \frac{4}{5}\frac{\nu}{\eta}. \tag{3.37}$$

Under the assumption that $c(\kappa)$ is monotonically decreasing, the result in equation (3.37) provides an analytical expression for the region of the parameter space where we expect signal transmission. In figure 7, we show that this expression matches the numerical results. Interestingly, equation (3.37) depends only on the ratio of the other parameters, ν/η. The scales of the horizontal axes for figure pairs figure 7*a*,*c* and *b*,*d* have been chosen to highlight this.

To gain information about the shape of $c(\kappa)$ near $\kappa = 0$, we pose a perturbation solution around $\kappa = \kappa_*$ to the system governed by equation (3.36) and the far-field relationship, equation (3.25), where

$$c = c_* + c_{\frac{1}{2}}\sqrt{\kappa_* - \kappa} + \mathcal{O}(\kappa_* - \kappa) \tag{3.38}$$

and

$$\mu = \mu_* + \mu_{\frac{1}{2}}\sqrt{\kappa_* - \kappa} + \mathcal{O}(\kappa_* - \kappa), \tag{3.39}$$

where μ_*, given by equation (3.33), and $c_* = 0$ apply at $\kappa = \kappa_*$. Substitution of these expansions into equations (3.25) and (3.36) gives

$$c_{\frac{1}{2}} = \sqrt{\frac{7}{5(\eta - 1)}}, \tag{3.40}$$

so that, for $\kappa \approx \kappa_*$,

$$c(\kappa) \sim \sqrt{\frac{7(\kappa_* - \kappa)}{5(\eta - 1)}}. \tag{3.41}$$

Figure 7 shows that equation (3.41) matches numerical results for $c(\kappa)$ for a surprisingly wide range of $\kappa < \kappa_*$, especially for larger η. This result is particularly important as we have not constructed a full perturbation solution to the travelling wave model about $c = 0$.

(iii) Combined approximation

We can combine the approximations to $c(\kappa)$ from the slow and the fast wave to obtain a curve that behaves like equation (3.29) for $\kappa \to 0$ and like equation (3.41) as $\kappa \to \kappa_*$. To do this, we propose a

form like

$$c(\kappa) \approx \alpha_1 + \alpha_2 \kappa + \alpha_3 \sqrt{\kappa_* - \kappa}, \tag{3.42}$$

where we choose

$$\alpha_1 = -(c_0 + 2\tilde{c}_1 \kappa_*), \quad \alpha_2 = \frac{c_0}{\kappa_*} + 2\tilde{c}_1 \quad \text{and} \quad \alpha_3 = \frac{2(c_0 + \tilde{c}_1 \kappa_*)}{\sqrt{\kappa_*}}, \tag{3.43}$$

where c_0 is given by equation (3.7); $\tilde{c}_1$ is given by equation (3.28); and κ_* is given by equation (3.37). In figure 7, we show that this combined approximation provides a reasonable approximation to $c(\kappa)$ for $\kappa \in [0, \kappa_*]$.

(iv) Whole domain ansatz

Results in equations (3.5) and (3.32) show that $f(z)$ is described exactly by a hyperbolic tangent at both $\kappa = 0$ and $\kappa = \kappa_*$, and figure 6*a* suggests that $f(z)$ remains sigmoidal. Therefore, it may be reasonable to approximate $f(z) \approx \tanh(\mu(\kappa) z)$ for $\kappa \in [0, \kappa_*]$, where $\mu(\kappa)$ depends on κ. Additionally, assuming that $\mu(\kappa)$ decays linearly from $\mu = \mu_0$ at $\kappa = 0$ to $\mu = \mu_*$ at $\kappa = \kappa_*$, we obtain an approximation to $f(z)$ for all κ,

$$f(z) \sim -\tanh(\mu(\kappa) z) \quad \text{and} \quad \mu(\kappa) = \frac{\mu_* - \mu_0}{\kappa_*} \kappa + \mu_0. \tag{3.44}$$

Substituting the approximation for $\mu(\kappa)$ given by equation (3.44) into the far-field matching condition (equation (3.25)) gives an approximation to $c(\kappa)$ which can apply for $\kappa \in [0, \kappa_*]$. We show that this approximation is reasonably accurate throughout $\kappa \in [0, \kappa_*]$ in figure 7; however, it is clear from numerical results in figure 6, when $\kappa = 0.4$, that the solution does not have the symmetry of a hyperbolic tangent function.

4. Discussion and conclusion

Currently, the inactive metamaterial described mathematically by Nadkarni *et al.* [4] and experimentally realized by Raney *et al.* [5] is able to transmit mechanical signals by the release of stored potential energy. A limitation of this design is that mechanical energy must be manually introduced into the system before additional signals can be transmitted. Our study presents a novel biologically inspired metamaterial that incorporates a theoretical biological mechanism that harvests energy to reset the system to a high potential energy state, allowing the transmission of additional signals. Energy may be induced into the active metamaterial through a biological process, such as actin filaments in eukaryotic cells [26–28]. That said, our analysis does not necessarily require this mechanism to have a biological origin: the reaction mechanism may also represent a mechanical system where energy is added through other electrochemical [44], photovoltaic, thermodynamic [20] or pneumatic [21] subsystems.

By finding evidence of travelling wave solutions, we are able to analyse limiting behaviour describing the signal transmission speed and wave shape. We provide a detailed analysis to qualitatively and quantitatively understand the effect of our reaction mechanism on signal transmission abilities of the material. Our main results consist of a set of analytical approximations that quantify the signal transmission speed as a function of the parameters which describe the physical properties of the material. Results in figure 7 show that the approximation we develop to apply through the whole domain, given by equation (3.42), provides an excellent match to the numerical results, particularly for large η. In addition, our approximation for the wavespeed near the slow wave, given by equation (3.41), is able to provide excellent information about the shape of $c(\kappa)$ as $c \to 0$, which we find is difficult to obtain numerically. This approximation is also able to provide a region of the parameter space for which signal transmission can occur, given by $\kappa < 4\nu/(5\eta)$ (equation (3.37)). This understanding of the effect of our mechanism on the signal transmission speed is useful as it allows our active metamaterial to be tuned to produce desirable new behaviours. For example, our results allow quantification

of the trade-off between signal transmission speed and the response time, which is essential for controlling the material. These insights are also essential for building a material containing a biological mechanism that induces energy into the system. Decreasing ν and η in the same proportion increases the transmission speed at the cost of increased sensitivity to noise-induced misfiring, but may be essential if the energy budget is small.

A key aspect of our study is to follow Nadkarni *et al.* [4] by representing the bistable potential energy function as a quartic (equation (2.2)). This approach leads us to obtain numerous analytical approximations that characterize the effect of the biological mechanism on the transmission speed which, although qualitatively reliable, may not always be quantitatively appropriate for particular systems [5]. In fact, the analytical expression for the transmission speed is a result of the similarity between our model and the well-studied bistable equation [38]. These choices mean that our system has mechanical and algebraic properties that are similar to other bistable systems, such as the FitzHugh–Nagumo model [31,33]. That said, we do not assume that the time scale of the response is significantly slower than the time scale of the excitement, as is often the case in analysis of such models. Indeed, our aim is to develop an intelligent biomechanical material that has tuneable properties. In some sense, it is desirable that the response is as fast as possible to allow for a short period of time between signal reception and retransmission. Future work may examine the role of heterogeneities in the properties of the material [3,45]. Such features could allow the material to selectively transmit signals by creating energy barriers that interact with signals of certain properties [13].

The travelling wave analysis we conduct assumes a material of infinite length over a large period of time. However, applications of our material will have a finite length and may have properties not suitable for a continuum model. For example, in a material where the spacing between elements is not significantly different from the length of the material, a discrete travelling wave analysis may be more appropriate. The discrete problem is known to be substantially more difficult than the continuous problem [38], so the limiting transmission speed our analysis provides may still be useful. Furthermore, the inclusion of our biologically inspired mechanism can be incorporated into passive metamaterials of higher dimensions to enable new behaviours and the travelling wave analysis can be extended to investigate two-dimensional signal propagation. In the electronic supplementary material, we produce results which show the transmission of concurrent signals (electronic supplementary material, figures S1 and S2) and interacting signals initiated from both ends of the material (electronic supplementary material, figure S3). Further analysis is needed to examine the behaviour of these types of interacting waves [46] and the material's ability to transmit oscillatory or concurrent signals.

To conclude, we have presented a novel, biologically inspired, active metamaterial that can reversibly transmit mechanical signals. This work provides an analytical expression that describes the mechanical properties of the material required for signal transmission. We also provide numerous approximations that quantify the effect of the mechanical properties, and the time scale of the biological response, on the transmission speed. This work demonstrates how a new class of biologically inspired metamaterials are able to produce useful new functionalities. The type of analysis we present is invaluable for tuning and controlling the active metamaterial.

Data accessibility. Additional data are provided in the electronic supplementary material. Key algorithms used to generate results are available on Github at github.com/ap-browning/rspa-2019.

Authors' contributions. All authors conceived and designed the study; A.P.B. performed the analysis and numerical simulations, and drafted the article; all authors provided comments and gave final approval for publication.

Competing interests. We declare we have no competing interests.

Funding. This work is supported by the Australian Research Council (DP170100474) and a Royal Society exchanges grant (no. IE160805).

Acknowledgements. We thank Kevin Burrage and Ian Turner for their helpful discussions. We also thank the three anonymous referees for their comments.

References

1. Bertoldi K, Vitelli V, Christensen J, van Hecke M. 2017 Flexible mechanical metamaterials. *Nat. Rev. Mater.* **2**, 17066. (doi:10.1038/natrevmats.2017.66)
2. Paulose J, Meeussen AS, Vitelli V. 2015 Selective buckling via states of self-stress in topological metamaterials. *Proc. Natl Acad. Sci. USA* **112**, 7639–7644. (doi:10.1073/pnas.1502939112)
3. Hwang M, Arrieta AF. 2018 Solitary waves in bistable lattices with stiffness grading: augmenting propagation control. *Phys. Rev. E* **98**, 042205. (doi:10.1103/PhysRevE.98.042205)
4. Nadkarni N, Daraio C, Abeyaratne R, Kochmann DM. 2016 Universal energy transport law for dissipative and diffusive phase transitions. *Phys. Rev. B* **93**, 1340–1347. (doi:10.1103/PhysRevB.93.104109)
5. Raney JR, Nadkarni N, Daraio C, Kochmann DM, Lewis JA, Bertoldi K. 2016 Stable propagation of mechanical signals in soft media using stored elastic energy. *Proc. Natl Acad. Sci. USA* **113**, 9722–9727. (doi:10.1073/pnas.1604838113)
6. Deng B, Wang P, He Q, Tournat V, Bertoldi K. 2018 Metamaterials with amplitude gaps for elastic solitons. *Nat. Commun.* **9**, 3410. (doi:10.1038/s41467-018-05908-9)
7. Kochmann DM, Bertoldi K. 2017 Exploiting microstructural instabilities in solids and structures: from metamaterials to structural transitions. *Appl. Mech. Rev.* **69**, 050801. (doi:10.1115/1.4037966)
8. Dudek KK, Gatt R, Dudek MR, Grima JN. 2018 Negative and positive stiffness in auxetic magneto-mechanical metamaterials. *Proc. R. Soc. A* **474**, 20180003. (doi:10.1098/rspa.2018.0003)
9. Serra-Garcia M, Molerón M, Daraio C. 2018 Tunable, synchronized frequency down-conversion in magnetic lattices with defects. *Phil. Trans. R. Soc. A* **376**, 20170137. (doi:10.1098/rsta.2017.0137)
10. Silverberg JL, Evans AA, McLeod L, Hayward RC, Hull T, Santangelo CD, Cohen I. 2014 Using origami design principles to fold reprogrammable mechanical metamaterials. *Science* **345**, 647–650. (doi:10.1126/science.1252876)
11. Paulose J, Chen B, Vitelli V. 2015 Topological modes bound to dislocations in mechanical metamaterials. *Nat. Phys.* **11**, 153–156. (doi:10.1038/nphys3185)
12. Turco E, Giorgio I, Misra A, dell'Isola F. 2017 King post truss as a motif for internal structure of (meta)material with controlled elastic properties. *R. Soc. open sci.* **4**, 171153. (doi:10.1098/rsos.171153)
13. Fang H, Wang KW, Li S. 2017 Asymmetric energy barrier and mechanical diode effect from folding multi-stable stacked-origami. *Extr. Mech. Lett.* **17**, 7–15. (doi:10.1016/j.eml.2017.09.008)
14. Deng B, Raney JR, Tournat V, Bertoldi K. 2017 Elastic vector solitons in soft architected materials. *Phys. Rev. Lett.* **118**, 204102. (doi:10.1103/PhysRevLett.118.204102)
15. Ion A, Wall L, Kovacs R, Baudisch P. 2017 Digital mechanical metamaterials. In *Proc. of the 2017 CHI Conf. on Human Factors in Computing Systems* (*CHI '17*), *Denver, CO, 6–11 May 2017*, pp. 977–988. New York, NY: ACM.
16. Matlack KH, Bauhofer A, Krödel S, Palermo A, Daraio C. 2016 Composite 3D-printed metastructures for low-frequency and broadband vibration absorption. *Proc. Natl Acad. Sci. USA* **113**, 8386–8390. (doi:10.1073/pnas.1600171113)
17. Chen T, Bilal OR, Shea K, Daraio C. 2018 Harnessing bistability for directional propulsion of soft, untethered robots. *Proc. Natl Acad. Sci. USA* **115**, 5698–5702. (doi:10.1073/pnas.1800386115)
18. Chen T, Mueller J, Shea K. 2017 Integrated design and simulation of tunable, multi-state structures fabricated monolithically with multi-material 3D printing. *Sci. Rep.* **7**, 45671. (doi:10.1038/srep45671)
19. Baardink G, Souslov A, Paulos J, Vitelli V. 2018 Localizing softness and stress along loops in 3D topological metamaterials. *Proc. Natl Acad. Sci. USA* **115**, 489–494. (doi:10.1073/pnas.1713826115)
20. Ding Z, Yuan C, Peng X, Wang T, Qi HJ, Dunn ML. 2017 Direct 4D printing via active composite materials. *Sci. Adv.* **3**, e1602890. (doi:10.1126/sciadv.1602890)
21. Wehner M *et al.* 2014 Pneumatic energy sources for autonomous and wearable soft robotics. *Soft Rob.* **1**, 263–274. (doi:10.1089/soro.2014.0018)
22. Wiktor V, Jonkers HM. 2011 Quantification of crack-healing in novel bacteria-based self-healing concrete. *Cem. Concr. Compos.* **33**, 763–770. (doi:10.1016/j.cemconcomp.2011.03.012)

23. Miniaci M, Krushynska A, Movchan AB, Bosia F, Pugno NM. 2016 Spider web-inspired acoustic metamaterials. *Appl. Phys. Lett.* **109**, 071905. (doi:10.1063/1.4961307)
24. Jiang Y, Korpas LM, Raney JR. 2019 Bifurcation-based embodied logic and autonomous actuation. *Nat. Commun.* **10**, 128. (doi:10.1038/s41467-018-08055-3)
25. Woodhouse FG, Ronellenfitsch H, Dunkel J. 2018 Autonomous actuation of zero modes in mechanical networks far from equilibrium. *Phys. Rev. Lett.* **121**, 178001. (doi:10.1103/PhysRevLett.121.178001)
26. Pollard TD, Cooper JA. 1986 Actin and actin-binding proteins. A critical evaluation of mechanisms and functions. *Annu. Rev. Biochem.* **55**, 987–1035. (doi:10.1146/annurev.bi.55.070186.005011)
27. Blanchoin L, Boujemaa-Paterski R, Sykes C, Plastino J. 2014 Actin dynamics, architecture, and mechanics in cell motility. *Physiol. Rev.* **94**, 235–263. (doi:10.1152/physrev.00018.2013)
28. Kumar S, Mansson A. 2017 Covalent and non-covalent chemical engineering of actin for biotechnological applications. *Biotechnol. Adv.* **35**, 867–888. (doi:10.1016/j.biotechadv.2017.08.002)
29. Nicolau Jr DV *et al.* 2016 Parallel computation with molecular-motor-propelled agents in nanofabricated networks. *Proc. Natl Acad. Sci. USA* **113**, 2591–2596. (doi:10.1073/pnas.1510825113)
30. Rouvala M, Amaratunga G, Wei D, Colli A. 2010 *Nanotechnologies for future mobile devices*. Cambridge, UK: Cambridge University Press.
31. FitzHugh R. 1955 Mathematical models of threshold phenomena in the nerve membrane. *Bull. Math. Biophys.* **17**, 257–278. (doi:10.1007/BF02477753)
32. Rubin J, Wechselberger M. 2008 The selection of mixed-mode oscillations in a Hodgkin-Huxley model with multiple timescales. *Chaos* **18**, 015105. (doi:10.1063/1.2789564)
33. Beck M, Jones CKRT, Schaeffer D, Wechselberger M. 2008 Electrical waves in a one-dimensional model of cardiac tissue. *SIAM J. Appl. Dyn. Syst.* **7**, 1558–1581. (doi:10.1137/070709980)
34. Baker RE, Parker A, Simpson MJ. 2019 A free boundary model of epithelial dynamics. *J. Theor. Biol.* (doi:10.1016/j.jtbi.2018.12.025)
35. Hwang M, Arrieta AF. 2018 Input-independent energy harvesting in bistable lattices from transition waves. *Sci. Rep.* **8**, 3630. (doi:10.1038/s41598-018-22003-7)
36. Billingham J, Needham DJ. 1991 The development of travelling waves in quadratic and cubic autocatalysis with unequal diffusion rates. I. Permanent form travelling waves. *Phil. Trans. R. Soc. Lond. A* **334**, 1–24. (doi:10.1098/rsta.1991.0001)
37. Murray JD. 2002 *Mathematical biology*. Berlin, Germany: Springer-Verlag.
38. Keener J, Sneyd J. 2009 *Mathematical physiology*. New York, NY: Springer.
39. Landman KA, Simpson MJ, Slater JL, Newgreen DF. 2005 Diffusive and chemotactic cellular migration: smooth and discontinuous traveling wave solutions. *SIAM J. Appl. Math.* **65**, 1420–1442. (doi:10.1137/040604066)
40. Simpson MJ, Landman KA, Hughes BD, Newgreen FD. 2006 Looking inside an invasion wave of cells using continuum models: proliferation is the key. *J. Theor. Biol.* **243**, 343–360. (doi:10.1016/j.jtbi.2006.06.021)
41. Nadkarni N, Arrieta AF, Chong C, Kochmann DM, Daraio C. 2016 Unidirectional transition waves in bistable lattices. *Phys. Rev. Lett.* **116**, 244501. (doi:10.1103/PhysRevLett.116.244501)
42. Nizovtseva IG, Galenko PK. 2018 Travelling-wave amplitudes as solutions of the phase-field crystal equation. *Phil. Trans. R. Soc. A* **376**, 20170202. (doi:10.1098/rsta.2017.0202)
43. Hinch EJ. 1991 *Perturbation methods*. Cambridge, UK: Cambridge University Press.
44. Snita D, Sevcikova H, Marek M, Merkin JH. 1997 Travelling waves in an ionic autocatalytic chemical system with an imposed electric field. *Proc. R. Soc. A* **453**, 2325–2351. (doi:10.1098/rspa.1997.0124)
45. Murphy RJ, Buenzli PR, Baker RE, Simpson MJ. 2019 A one-dimensional individual-based mechanical model of cell movement in heterogeneous tissues and its coarse-grained approximation. *Proc. R. Soc. A* **475**, 20180838. (doi:10.1098/rspa.2018.0838)
46. Simpson MJ, Landman KA, Bhaganagarapu K. 2007 Coalescence of interacting cell populations. *J. Theor. Biol.* **247**, 525–543. (doi:10.1016/j.jtbi.2007.02.020)